Microsc. Microanal. 23, 647–660, 2017
doi:10.1017/S1431927617000435

Microscopy AND Microanalysis

Pattern Center and Distortion Determined from Faint, Diffuse Electron Diffraction Rings from Amorphous Materials

János L. Lábár,[1,*] and Partha P. Das[2]

[1]*Centre for Energy Research, Institute of Technical Physics and Materials Science, Hungarian Academy of Sciences, H-1121 Budapest, Konkoly-Thege M. u. 29-33, Hungary*
[2]*Electron Crystallography Solutions, Orense 8, 28032 Madrid, Spain*

Abstract: Diffuse rings from amorphous materials sit on a steep background resulting in a monotonically decreasing intensity over scattering vector length, frequently with no clear local maximum that could be used to determine the center of the ring. The novelty of the method reported here is that it successful processes such weak patterns. It is based on separating the angular dependence of the positions of the maxima on the azimuthal angle in the measured two-dimensional pattern for a manually preselected peak. Both pattern center and elliptical distortion are simultaneously refined from this angular dependence. Both steps are based on nonlinear least square fitting, using the Levenberg–Marquardt method. It can be successfully applied to any amorphous patterns provided they were recorded with experimental conditions that facilitate dividing them into sectors with acceptable statistics. Patterns with the center shifted to the camera corner (recording a quadrant of a ring) can also be reliably evaluated, keeping precalibrated values of the elliptical distortion fixed during the fit. Finally, the limited number of counts in any pattern is overcome by cumulating many patterns (from equivalent areas) into a single pattern. Eliminating false effects is facilitated by masking out unwanted parts of any recorded pattern from processing.

Key words: TEM, thin films, computer program, partial patterns, amorphous materials

Introduction

Electron diffraction patterns recorded from thin films in a transmission electron microscope (TEM) carry a wealth of information. However, extraction of quantitative data from them is based on the accurate knowledge of the pattern center and the size and orientation of elliptical distortion. It is, therefore, not surprising that the last decade saw a continual effort to determine these parameters and correct for their effects (Lábár, 2000, 2002, 2005, 2008, 2009; Lábár & Adamik, 2001; Capitani et al., 2006; Li, 2007; Hou, 2008; Mitchell, 2008*a*, 2008*b*; Carvalho & Morales, 2012; Wu et al., 2012; Klinger & Jager, 2015; Klinger et al., 2015; Mitchell & Van den Berg, 2016). Although all of them have their own success for solving part of the problem, some room was still left for improvement. Different approaches are followed for single-crystal spot patterns on the one hand and ring patterns from nanocrystalline (nc) or amorphous materials on the other. Locating spots or rings and refining pattern center and elliptical distortion are central to all the procedures.

For single-crystal patterns (Wu et al., 2012) identifies the spots with iterative cross-correlation with a circular mask, identifies the two shortest nonlinear vectors and ascribes the center of the pattern to the brightest spot. Jansen (2006) used a double polynomial for the correction of the positions of single-crystal diffraction spots. Belletti et al. (2000) fitted an approximate grid of straight lines to the measured points. Klinger & Jager (2015) fit a regular lattice to the spots, which are identified by blob detection to locate the center, whereas Klinger et al. (2015) uses circular Hough transform (CHT) to locate convergent beam electron diffraction (CBED) disks. Klinger et al. (2015) determines disk centers separately for each depicted CBED disk using Hough transform, then finds a regular lattice best fitting those ring centers which actually refines positions of the disk centers and, finally, the refined disk center closest to the intensity-weighted centroid of the image is taken as the pattern center. Lábár (2005) identifies two short vectors manually and the program automatically finds the center of gravity in pre-selected surroundings of both the identified spot and its mirror image (relative to the assumed center) and refines center position to the bisector of these two lines. A very similar approach is named "d-spacing-d-spacing measurement option" in Mitchell (2008*b*), where pattern center was also ascribed to the bisector of the two short vectors. As a starting rough estimate for pattern center, Lábár (2005) also offers computing the center of gravity of a region close to the center of the image and makes the subsequent automatic, brute-force refinement form that position. Mitchell (2008*b*) and Mitchell & Petersen (2012) offer four different approaches to obtain the first rough estimate, including simple or

Received August 17, 2016; accepted March 9, 2017
*Corresponding author. labar.janos@energia.mta.hu

thresholding the patterns and a brute-force method. For manual determination of the first estimate of the pattern center (Lábár, 2000, 2002, 2005, 2008, 2009; Lábár & Adamik, 2001) offers visual comparison to a reference circle, while the pattern can be shifted until the symmetrically equivalent points are seen on the reference circle with variable radius. Mitchell (2008*b*) offers a similar manual possibility with several reference circles generated simultaneously on screen.

As far as the ring patterns are concerned, most of the methods require some user interaction whereas the fully automatic CHT approach of Mitchell (2008*a*) determines the pattern center accurately, but cannot deal with elliptical distortion. Klinger & Jager (2015) computes the difference between the original pattern and ones rotated around preassumed pattern center and minimize the difference by refining the center. Lábár (2000, 2002, 2008, 2009) and Lábár & Adamik (2001) determines both pattern center and elliptical distortion by manually overlaying a circle or an ellipse on the pattern and adjusting its parameters till good visual match is attained. Li (2007) computes intensity profiles both horizontally and vertically to obtain both pattern center and elliptical distortion. Each step in his paper can be compared with the solutions in Lábár (2000), which was used in many laboratories that time, proved by the large number of independent citations to that paper. Hou & Li (2008) recommend adjusting the stigmators of the TEM lenses to a "diffraction-optimal" condition, a hardware solution to eliminate elliptical distortion. Unfortunately the recommended condition produces highly distorted images as a price for distortion-free diffraction patterns. The experimentally determined elliptical distortion is used differently in different programs. Lábár (2000, 2002, 2005, 2008, 2009) and Lábár & Adamik (2001) uses the parameters of the visually adjusted ellipse to calculate an equivalent circular radius (which is the root mean square of the major and minor axis lengths of the ellipse) for calculating the one-dimensional (1D) intensity distribution (intensity versus radius), but does not warp the image to render a corrected pattern. Li (2007) and Mitchell & Van den Berg (2016) not only use the corrected distance for generating the intensity distribution but also additionally warp the pattern to restore accurate circular appearance. Even the determination of the parameters of the ellipse is done differently by the individual authors. The parameters of the ellipse were determined by fitting the bright spots of a diffraction ring within a band (with manually preselected width) around a preselected reference circle in Lábár (2009), although the mathematical formulas for the canonical form of the shifted and rotated ellipse were not elaborated in his publication, as these equations were simply taken from a math textbook. Mitchell & Van den Berg (2016) went further, on one hand they published each detailed step of an elaborated ellipse-fitting procedure and fitted to several rings simultaneously. On the other hand they also introduced an important further step, namely the elimination of outer points (very high order reflections), which improved both robustness and accuracy. In addition, their procedure determines pattern center and elliptical distortion simultaneously. All these procedures were tested on polycrystalline rings that emerged significantly from the background (BKG) and were narrower than those encountered in amorphous materials. These methods were also able to handle incomplete rings (due to either spottiness or the presence of a beam-stop). The faint and broad (varying width) rings, over an intense and steep BKG, from amorphous materials require different treatment, which is the topic of the present paper. An additional complication is that sometimes the (BKG) intensity is not uniform around the center (similar to, but not as strong, as that observed, e.g., in wedge-shaped samples), which calls for sector-wise treatment instead of applying a BKG determined from the azimuthally averaged 1D intensity distribution [e.g., to remove it from the measured two-dimensional (2D) pattern] (see Fitting a Small, Diffuse Peak on a Steep BKG section).

Transformation to polar coordinates is a central idea to some procedures (Capitani et al., 2006; Hou, 2008; Carvalho & Morales, 2012). Capitani et al. (2006) plot the ratios between observed and average interplanar spacings for symmetry related spots versus orientation measured from the reference horizontal x-axis and fit a sinusoidal curve to it to determine the parameters of the ellipse. However, they take the center of the pattern for granted; Carvalho & Morales (2012) re-plot the pattern in polar coordinates and make measurement of lattice spacings along individual angular values. Hou & Li (2008) find the center and the distortion in two distinct steps. They first locate the center by minimizing the difference between all points along the ellipse and their mirror points, which is seen as a generalization of the procedure by Lábár (2005) to more points. Next they fit an elliptical function in polar coordinates to determine distortion. However, this procedure also assumes well-located ring-maxima.

When incomplete rings are mentioned in the literature, it usually means spotty rings, small missing sections or the pattern partially covered by a beam-stop. Significantly shifted ring patterns (e.g., with center in the corner of the charge coupled device [CCD]) are not examined in the above publications. The difficulty with such patterns is that only a small segment (slightly more than a quadrant) is recorded that produces a great deal of complication. The algorithm described by Mitchell & Van den Berg (2016) should not have any principal problem with such patterns, however, it is not tested in his paper. The present paper also treats possibilities and limitations with such partial patterns.

Unwanted features in the patterns (shadow of beam-stop, numbering, size-marker, etc.) are masked out in several programs, but they treat the problem differently. Klinger & Jager (2015) replaces the masked region with a circular average that produces nice visual appearance in regions, which in reality do not contain useful measured information. The masked out pixels in the present paper are left out from processing by setting their values to 0.

Different functional forms are used in the literature to describe the dependence of the BKG intensity on the length of the scattering vector in rotationally (azimuthally) averaged intensity distributions. The polynomial functions used by X-ray diffraction programs do not seem to be satisfactory

for electron diffraction. Klinger & Jager (2015) use a hyperbolic function. There are several options in the ProcessDiffraction program (Lábár, 2008, 2009), namely a flexible cubic spline, a Gaussian function (named "normal" there), and the function selected here [equation (1)], which is called "log-normal" by Lábár (2008, 2009). It seems to fit to the BKG in case of many measured patterns over an extended range of scattering angle. In this paper it is only used in a limited range, covering the two sides of a diffuse ring.

As can be seen three main problems remain for amorphous materials. First, a procedure is needed to determine and refine the position of faint, diffuse rings that do not give well resolved local maxima over the steep BKG. Second, simultaneous determination of pattern center and elliptical distortion is desirable for broad, faint rings of amorphous materials (with similar quality as was solved for polycrystalline rings). Third, patterns with center in the corner of the camera field are also to be calibrated. These problems, together with the problem of a huge number of patterns with extremely low counts in many pixels (especially at the outer edges) and with slightly jumping centers are discussed in the present paper.

Principles and Implementation

The sections below discuss the problems in the logical sequence of processing the patterns. First the unwanted regions are removed by masking. Next the faint, diffuse rings are identified and quantified. Third, the pattern center and the elliptical distortion are simultaneously refined from the data of the faint rings. Finally, several such patterns recorded from dose-limited samples are cumulated or summed to improve statistics and make any tiny signal to emerge from the noise. In such patterns the more intense region of the pattern is used for identifying and refining the faint rings and performing the previously listed operations, whereas the least intense regions gain the most from summing them.

Masking Out Unwanted Parts of the Recorded Pattern

The recorded pattern may contain several components that are superimposed incoherently, so they may be removed without affecting the information content of the rest of the pattern. That category involves not only the trivial beam-stop shadow (Fig. 1), but also true diffraction components, which originate from unwanted parts of the sample as shown below. Separation of them is of general importance and not limited to the case of patterns where the useful information is in the form of faint diffuse diffraction rings. Such a case is presented in Figure 1 and discussed in Effect of Masks section. In the current implementation a composite mask is built from rectangles, circles, and polygons. An arbitrary number of these elements can be added to a composite mask. As the components to be masked out show a wide variety of size, shape, and position, their identification is manual (except for the automatic masking out of the central cross in a new TimePix detector (Amsterdam Scientific Instruments, Amsterdam, The Netherlands), which for the time being, contains false intensities at the edges of the four quadrants.). Individual mask elements can be drawn by the mouse on screen, or in the special case of the lattice of spots from a single-crystalline part of the sample, they can be generated by identifying the two shortest diffraction vectors pointing to two of these spots. Another example of automatic generation of a mask element is the TimePix detector, which shows a bright cross in its center as a detector artifact. Since the position of the artifact is fixed, it is masked out automatically. This especially increases processing speed and improves reproducible processing when a huge number of patterns from this detector are accumulated into a single pattern (see Fig. 2 in Limits of the Approaches section).

The pixels covered by the mask are left out when rotational averages are computed.

Fitting a Small, Diffuse Peak on a Steep BKG

The processing starts similarly to all ring patterns. First a rough estimate of the center for the 2D patterns is specified then the pattern is azimuthally (i.e., rotationally) averaged around this center to obtain a 1D distribution (intensity versus the distance from the center). The initial rough estimate for the center can be obtained either as an intensity-weighted position (center of gravity) or, alternatively, adjusted manually using a reference circle as in Lábár (2000). This rough estimate can automatically refined by a brute-force method as in Lábár & Adamik (2001) or, alternatively, by calculating the weight of gravity within the reference circle of preselected radius in the present version. Identification of rings is not a problem for well-developed rings that produce significant peaks in the rotationally averaged intensity distribution. However amorphous samples frequently produce faint rings, which do not create local maxima in the rotationally averaged intensity distribution as exemplified in Figure 3. In addition, the width of such a ring can also vary widely (in contrast to the limited range of width encountered with crystalline materials), preventing us from using a universal setting for the parameters of a top-hat filter for usual peak-find procedures and making initial manual interaction advisable. In the present procedure, the peak is identified by manual selection of two BKG intervals on its two sides. The smooth continuous curve in Figure 3 is the rotationally averaged intensity (of the measured pattern in Fig. 2a) over the entire circle and the BKG fitted to it is shown by a dotted line. An intensity averaged over a sector of the circle only [in the (25–30°) angular range measured from the horizontal, right-pointing vector] is also shown as a noisy curve with many false local maxima and minima. Automatically locating and especially quantifying such a faint and noisy peak (in 1D or the corresponding ring in 2D) over a steep BKG is a challenge to any of the existing methods. In addition to these problems, the BKG may not be evenly distributed azimuthally (as in Fig. 4). That small deviation from the perfect rotational symmetry does not increase significantly the error of net intensities when strong rings from

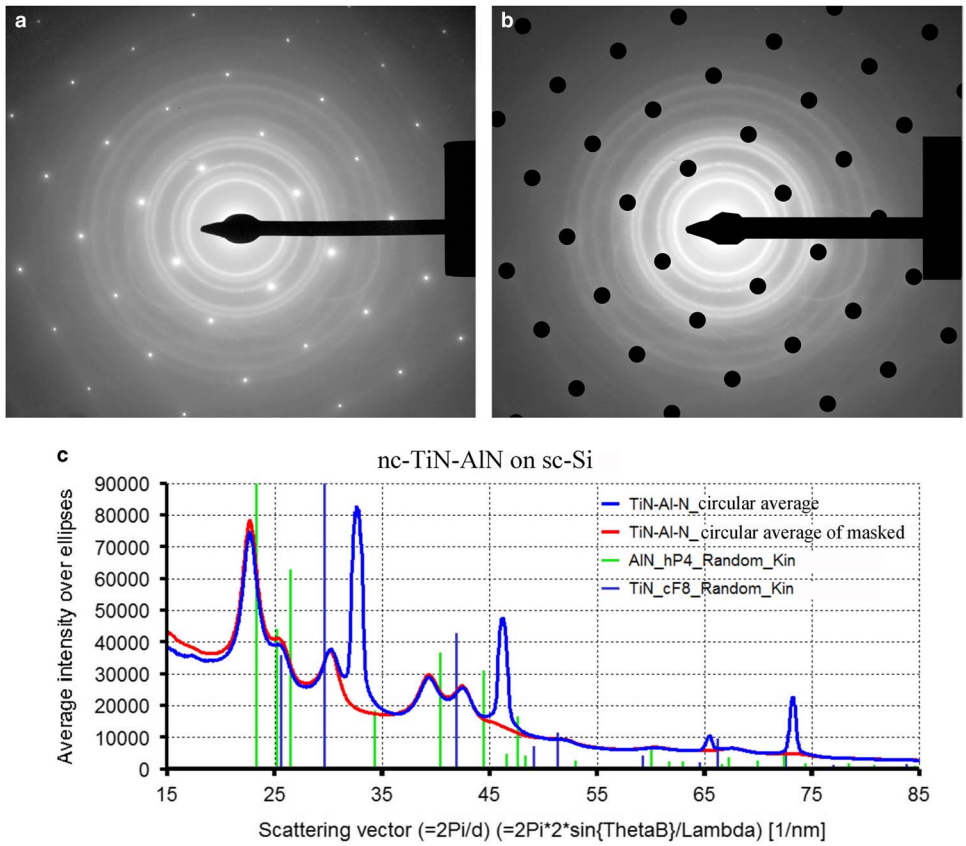

Figure 1. Diffraction rings from nanocrystalline TiN–AlN thin film on a single-crystal silicon (sc-Si) substrate. The shadows of both a Beam-stop and a numbering unit are seen together with the incoherent superposition of single-crystal diffraction spots from the incompletely removed Si substrate below. **a:** The original diffraction pattern. **b:** The masked version that removed both the shadows and the effect of the substrate. **c:** Comparison of rotationally averaged intensity distributions without and with masking. Phase composition can only be determined from the latter one. nc, Nanocrystalline.

crystalline materials are present. However, with our faint rings that small deviation is a problem for sector-wise processing. In our procedure, a faint peak is visually identified in the intensity distribution rotationally averaged over the entire circle and two BKG intervals are manually selected on its two sides. Then the pattern is re-processed sector-wise using these same intervals to quantify the ring-sectors.

The Levenberg–Marquardt method (Press et al., 1996) for nonlinear fitting is selected in this paper to fit both the BKG and the peak simultaneously to such measured 1D intensity distributions. The empirical function of equation (1) from Lábár (2008, 2009) is used to describe the shape of the BKG.

$$y = \exp\left(a_1 \cdot \log\{x\}^2 + a_2 \cdot \log\{x\} + a_3\right). \qquad (1)$$

The peak over this BKG is modeled by a Gaussian function. The nonlinear fit is done in two steps. The first step provides a good starting value for the second. First the two BKG intervals on the two sides of the peak are only used to fit with the function in equation (1). The endpoints of the two BKG intervals are indicated by asterisks in Figure 3. A first estimate of the net peak is calculated, using this fitted BKG, by numerical summation over the points within the BKG intervals. In the second step both the BKG (which is a function of $\log\{x\}$) and the Gaussian (which is a function of x) are fitted simultaneously to provide a better model of the total measured data in each sector.

To provide useful values for the next step (in the Different Dependence of the Measured Distance from the Center on a Small Shift in the Position of the Assumed Center and on Elliptical Distortion section) the entire 2D pattern is divided into sectors, using an initial estimate of the pattern center. The BKG intervals in the 1D distribution are selected only once (by clicking on the endpoints of the interval) on the intensity distribution recorded over the entire pattern. The same BKG intervals are reapplied automatically here to all sectors (e.g., 90 sectors in the case of 4° sector width for a complete circle). The sector width (azimuthal extent) is manually preselected. The fitting procedure above is carried out in each sector independently. Each sector is labeled with the azimuthal angle (at its center) measured from the right-pointed horizontal line and the position of the fitted peak is plotted as a function of this azimuthal angle (see Fig. 5). The resulting set of angle-position data pairs serves as input for Different Dependence of the Measured Distance from the

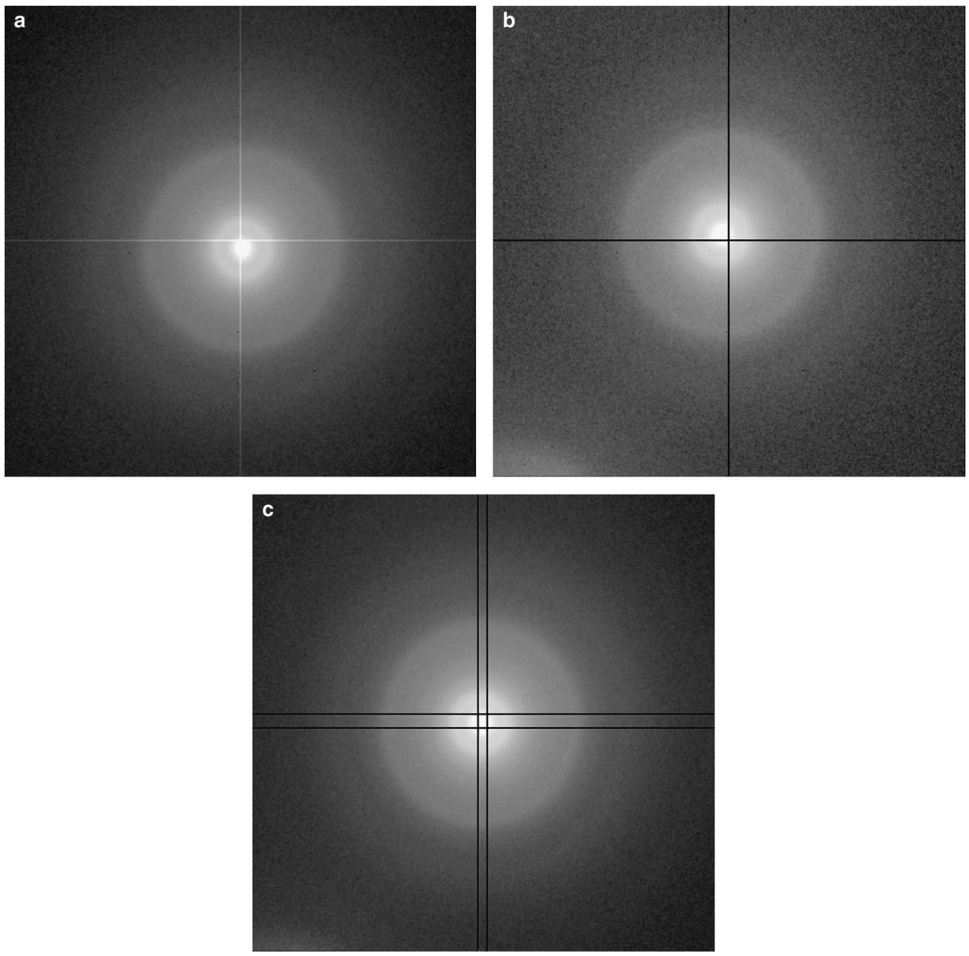

Figure 2. Example of summing (cumulating) two diffuse patterns. **a:** Faint diffuse pattern recorded from an amorphous aerosol thin film on a TimePix camera. The bright cross is a recording artifact of the camera. The artifact is not masked out to show it. **b:** A similar pattern from a different area of the same sample. The bright cross artifact is masked out. **c:** The cumulated, masked version. As the pattern centers were at different positions relative to the bright cross artifact at the individual patterns, two cross-shaped regions must be masked out at the final result when the pattern centers are shifted together. The size of the final patter is slightly reduced (502 × 497 pixels in contrast to the original 512 × 512), as only the common pixels are kept.

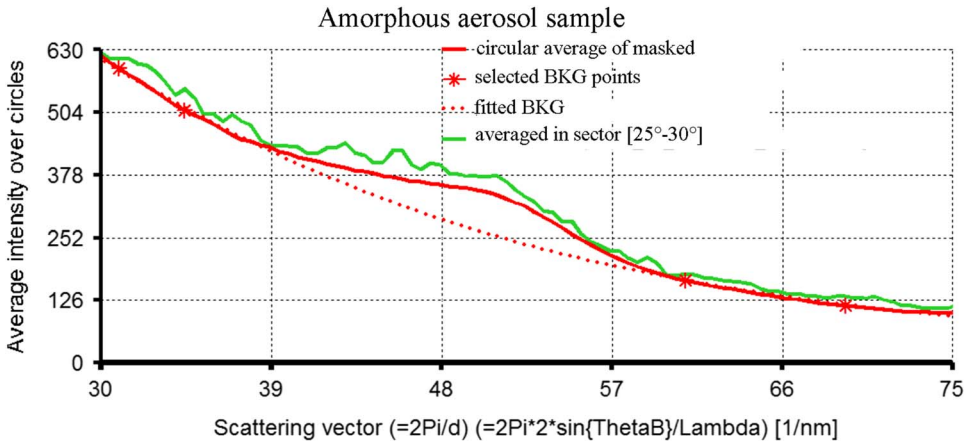

Figure 3. Example of rotationally averaged version of a faint, diffuse ring that does not produce local maximum in this one-dimensional representation. Calculated from the measured two-dimensional pattern in Figure 2a. BKG, background.

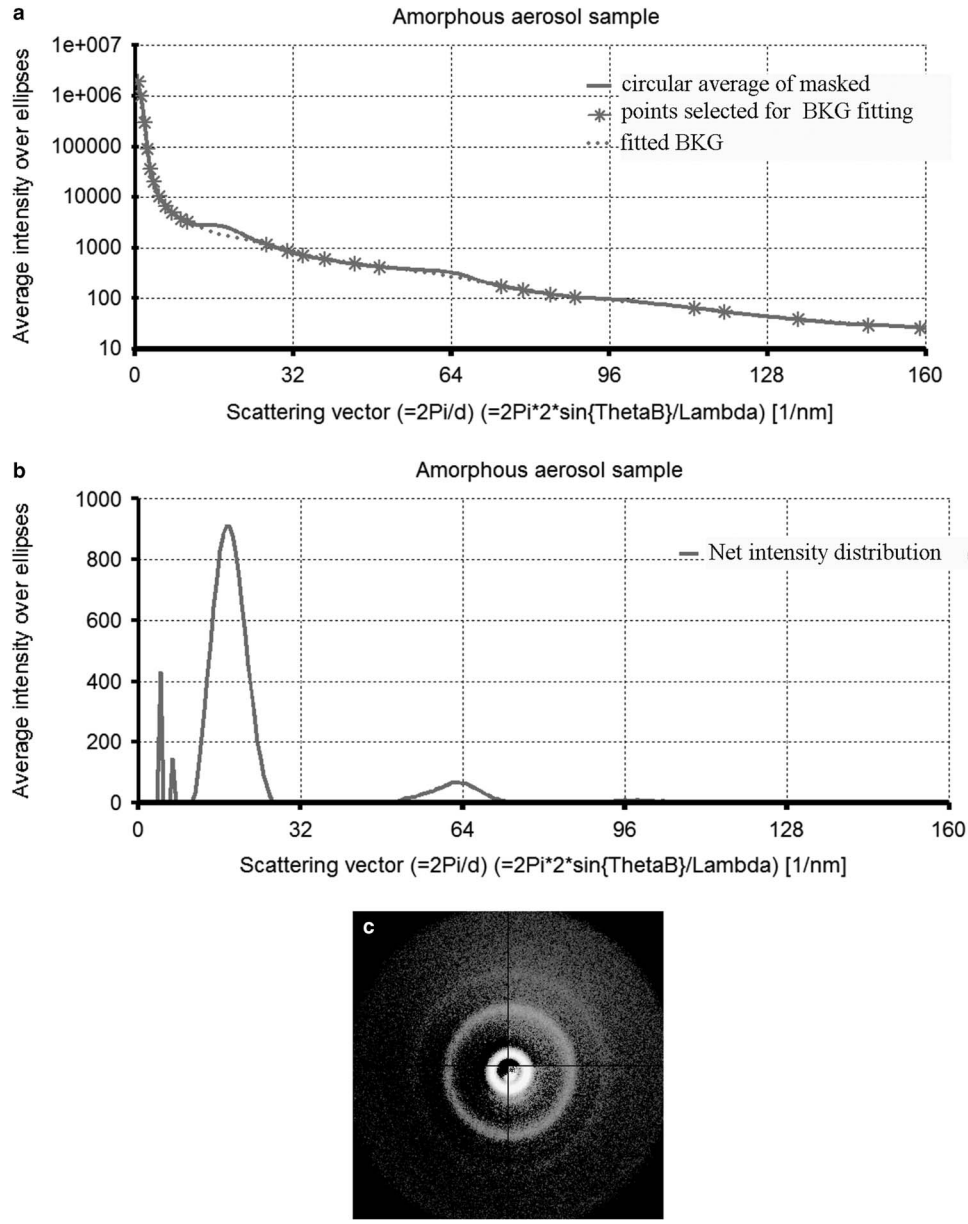

Figure 4. An example why sector-wise processing is preferred to background (BKG) subtraction method for faint diffuse rings over large and slightly uneven BKG. Slight deviation of the BKG from perfect circular symmetry results in errors, comparable with the peak of interest. **a:** Circularly averaged intensity over the entire circle (logarithmic scale) together with the fitted BKG. **b:** The net peaks calculated from (**a**), shown in a linear scale. **c:** The net two-dimensional pattern after having removed a circularly uniform BKG determined in (**a**). Deviation from rotational symmetry becomes significant. The effect of the same small deviation would be negligible if strong rings from polycrystalline materials were measured.

Center on a Small Shift in the Position of the Assumed Center and on Elliptical Distortion section.

Different Dependence of the Measured Distance from the Center on a Small Shift in the Position of the Assumed Center and on Elliptical Distortion

Separation of the two effects is based on the fact that they have different, well-defined periodicities. When the pattern is shifted in any direction the distances of maxima will be increased in that direction and reduced in the opposite direction. As the points along the circle are evaluated one-by-one, they follow a $\cos(\alpha)$ function, where α is the azimuthal angle of the measured point. If the pattern is elliptically distorted, there will be two long and two short distances as they follow each other by 90° separation, so the distance measured from the center is described by a $\cos(2\alpha)$ function. Phase shifts on both cases represent the orientation of the deviation. The two effects together are modeled by equation (2).

$$r = r_0 + A_1 \cos(\alpha + \varphi_1) + A_2 \cos(2\{\alpha + \varphi_2\}). \qquad (2)$$

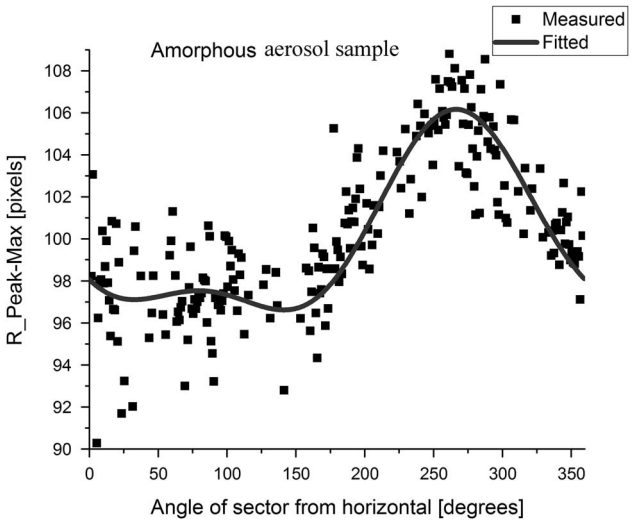

Figure 5. Angular dependence of the peak positions (squares) measured sector-by-sector form the amorphous pattern in Figure 2a using the procedure described in Fitting a Small, Diffuse Peak on a Steep BKG section. The continuous line is the fitted function used to determine both shift of the center and the elliptical distortion simultaneously (see Different Dependence of the Measured Distance from the Center on a Small Shift in the Position of the Assumed Center and on Elliptical Distortion section). Both effects are significant in the figure.

The five parameters are fitted simultaneously by the Levenberg–Marquardt method (Press et al., 1996). r_0 gives the true radius of the circle. The shift of the circle is given by equation (3a), whereas the numerical eccentricity by equation (3b). The orientation of the major axis of the ellipsis is given by φ_2.

$$dx = A_1 \cos(\varphi_1) \quad dy = A_1 \sin(\varphi_1), \tag{3a}$$

$$\epsilon = \sqrt{1 - \left\{\frac{r_0 - A_2}{r_0 + A_2}\right\}^2}. \tag{3b}$$

That functional form is fitted automatically to the data from Fitting a Small, Diffuse Peak on a Steep BKG section. Depending on the relative values of the two amplitudes and the two phase shifts, very different functional forms result. An example of the fitted function is seen in Figure 5.

Cumulating Several Patterns

In addition to improving statistics by increasing the number of counts per pixel, it is also desirable sometimes to increase the probed volume, e.g. when electron diffraction is to be compared with X-ray diffraction to see the behavior of the average. Although in most cases the advantage of TEM is to see the local in contrast to the average, sometimes examination of the average is also needed. Probing a large volume is impossible in any single patterns in the TEM. The only way to reach that goal is to collect many diffraction patterns from areas that should be identical and sum (cumulate) their information content. Such a series of patterns is frequently collected by automatic beam-scanning procedures and the number of patterns in any one set varies between 1,000 and 2,000, usually each with poor statistics for beam sensitive materials and occasional small jumps in the position of the center. Usual noise reducing cumulating procedures are only designed to unify a few patterns of varied exposure time and are not able to deal with beam-stepping, etc. The procedure presented here was developed for automatically cumulating a huge number of patterns after having refined their centers individually. As the patterns are usually measured in a session without significant changes to the lenses and the distortion depends on the lens settings, the elliptical distortion is the same for a series of patterns. As far as the masked regions are concerned, a region masked in any one of the patterns must be omitted from the total. In that way the total will be a collection of pixels collected with the total dose valid for the entire set of patters (sum of the individual doses), while any one measured spatial region of the sample received only a limited dose. Figure 2c shows such a masked cumulated pattern with the combined effect of the individual masks. The black pixels are left out of further processing.

Results and Discussion

Materials and Methods

Experimental patterns were collected from a TiN–AlN nc layer over a Si single-crystal substrate in a Philips CM-20 TEM (Philips, Eindhoven, The Netherlands) operated at 200 kV. The patterns were recorded on Ditabis imaging plates, which record intensity linearly over 20 bits dynamic range. An amorphous Si_3N_4 thin film and nc-Ni film were measured in a JEOL3010 TEM (JEOL, Tokyo, Japan), operated at 300 kV and the patterns were recorded on a GATAN Orius CCD camera (GATAN, Pleasanton, CA, USA). Some of the amorphous patterns were recorded from an amorphous aerosol with a TimePix detector on a CM-30 TEM (Philips, Eindhoven, The Netherlands) operated at 200 kV. Simulated rings with well-defined parameters were also used in a special test. All processing was done with the ProcessDiffraction program (Lábár, 2000, 2005, 2008, 2009) using the new features described in the present paper.

Effect of Masks

Even the simplest beam-stop, namely a wire with constant thickness gives a shadow, which covers different fractions of the entire circle if the circles with different radiuses are taken. That is why its effect is a function of the scattering angle and must be taken into account.

A more important example is shown in Figure 1. The sample is the same, which is used in a publication of Barna's group (Székely et al., 2014). It is shown in Lábár (2008, 2009) that phase fractions and preferentially oriented (textured) fractions can be determined from the rotationally averaged continuous rings recorded from nc thin films. However, the procedure assumes that the measured peaks in the 1D distribution (that corresponds to the rings in the 2D pattern) originate from the nc material alone. In the example in Figure 1 the nc-AlN–TiN composite film was grown on a native oxide covered single-crystal silicon (sc-Si) substrate. In order to

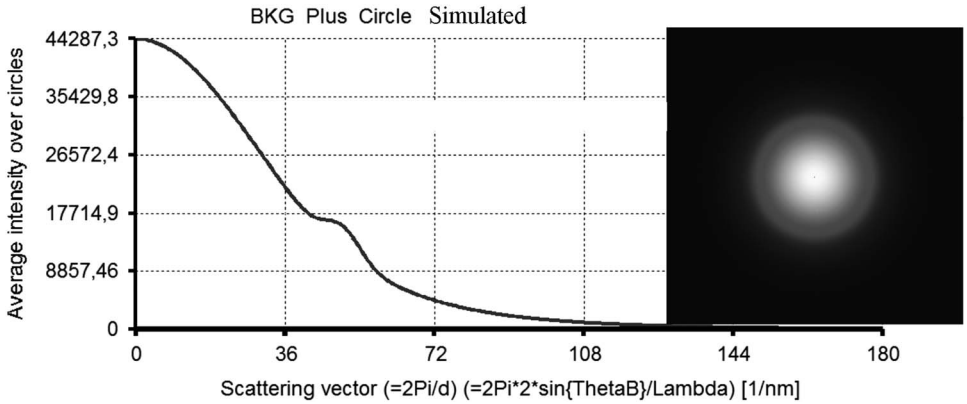

Figure 6. Simulated diffraction pattern and the distribution calculated from it by circular averaging. The parameters of simulation are very similar to a true measurement. No noise, known parameters. It serves as a test-bed both for fitting the BKG + peak and for the refinement of center and distortion.

be able to examine larger volume of the thin (20 nm) film the substrate was back-thinned till perforation to produce a plan-view sample with nominally self-supporting parts of the nc film close to the perforation. However, the recorded diffraction pattern in Figure 1a shows that the substrate was not removed perfectly and its spot pattern incoherently superposed over the pattern of the examined film. The rotationally averaged distribution (in Fig. 1c) was dominated by the strong reflections of the sc-Si, hindering (semi)quantitative evaluation of the pattern. Figure 1b shows how a lattice was generated from the manually identified two shortest diffraction vectors to produce a mask with disks of predefined radiuses. Although a non-negligible area fraction of the pattern is discarded this way, a large enough fraction of each ring still remained for processing (rotational averaging) shown in Figure 1c. Uniformity of the original rings ensured that the rotational average is the same irrespective of whether they were computed from these clean sections of the rings or if they had been computed from an entire clean ring. This corrected distribution (from the masked pattern) was appropriate for phase evaluation. The pattern was calibrated with the sc-Si spots, so it became obvious from Figure 1c that the diffraction lines of both the cubic silicon nitride and the hexagonal aluminum nitride phase were significantly shifted from their nominal values (indicated as "Marker-lines" named AlN_hP4_Random_Kin and TiN_cF8_Random_Kin[a] in Fig. 1c). The shift is caused by mutual solution of Al in cubic TiN and Ti in hexagonal AlN. Because of the different crystal structures of these two phases the Vegard-law cannot be applied, so the amount of dissolution cannot be quantified from the diffraction directly. The observed shifts are in accordance with the empirical atomic radii (125 pm for Al and 140 pm for Ti). Dissolution of the larger Ti increases the lattice constant of the AlN, resulting in a shift of the ring to the shorter diffraction vectors. For the dissolution of Al into TiN produces the shift in the opposite direction. It is possible to determine with the ProcessDiffraction program (Lábár, 2008, 2009) the relative volume fraction of the two phases, the volume fraction if preferentially oriented and the shift of the diffraction lines. Such analysis is impossible if the effect of the substrate spots are not removed by masking.

[a] The name of the calculated Marker lines contain the name of the phase, its structure and the fact that calculation assumed random orientation distribution of such small grains that kinematical approximation is expected to prevail.

Test on Simulated Patterns: Robustness and Accuracy

The simplest basic test is when a simulated pattern, without noise, is processed to see to what extent the known parameters of the center and elliptical distortion are confirmed.

First, a full circle on a steep BKG was generated. Figure 6 shows a pattern simulated with parameters very similar to a true measurement. The main difference is that all parameters are exactly known and there is no noise. The true center of the circle is at xc = 256, yc = 260 in the 512 × 512 pixel sized pattern. Processing was started from an assumed center of xc = 259, yc = 255. The true center was found with an indication of tiny elliptical distortion of <0.1% (i.e., deviation from the true radius of the circle of 100 pixels with 0.09 pixel, corresponding to $\varepsilon = 0.06$ instead of 0).

Next a similar full pattern with simulated elliptical distortion was generated. The parameters of the simulation were xc = 256, yc = 260, $\varepsilon = 0.25$, $\alpha = 70$ (parameters that resemble real life, but visually hard to distinguish from the pattern in Fig. 6). The refinement procedure was again started from xc = 259, yc = 255 with sector width = 2° and both the pattern center and the elliptical distortion parameters were refined. Again, all parameters were retrieved with sub-pixel accuracy (xc = 255.91; yc = 259.95; $\varepsilon = 0.249$; $\alpha = 71.6$). When the procedure was re-started from the newly found approximation of the center, it resulted in xc = 255.96; yc = 260.01; $\varepsilon = 0.252$ and $\alpha = 70.3$, proving that the procedure is convergent and does not change when the true parameters were found.

Both the above tests demonstrate perfect functioning of the process on simulated full patterns that result in the true values for both the center and the elliptical distortion with sub-pixel accuracy. Next, the effect of incompleteness (large missing sectors) was examined.

As a third simulation test an elliptical pattern was generated with the true center in the corner of the simulated area,

with xc = 5, yc = 502, $\varepsilon = 0.25$, $\alpha = 70$ to see if slightly more than a quarter of a circle (ellipse) is enough to find the true parameters. As shown below, fit to these partial data results the same sub-pixel accuracy only if the elliptical distortion is precalibrated and kept fixed during the refinement of the center. Otherwise a systematic error of a few pixels will be present, whose value depends on the starting conditions.

For this test, the refinement procedure was started with four different starting and boundary conditions. First, the procedure was started from a slightly shifted assumed center (xc = 1, yc = 498) with sector width = 2° and both the center and the elliptical distortion was fitted simultaneously (Fig. 7a). The result (xc = 2.29; yc = 504.73; $\varepsilon = 0.227$; $\alpha = 94.9$) showed a systematic error, which amounted to 2–3 pixels. It is not critical, and it is not surprising that such a partial data set cannot give perfect results even if there is no noise present. To test the reproducibility and convergence the procedure was re-started from the results of the previous fit. As seen in Figure 7b the previous result was reproduced with sub-pixel accuracy, indicating both that the procedure is convergent and that the small error is systematic in nature and arises from the interaction of the two functions (the measured deviation cannot be de-coupled unambiguously into the two cosine functions if the measured values are available only in a very limited angular range).

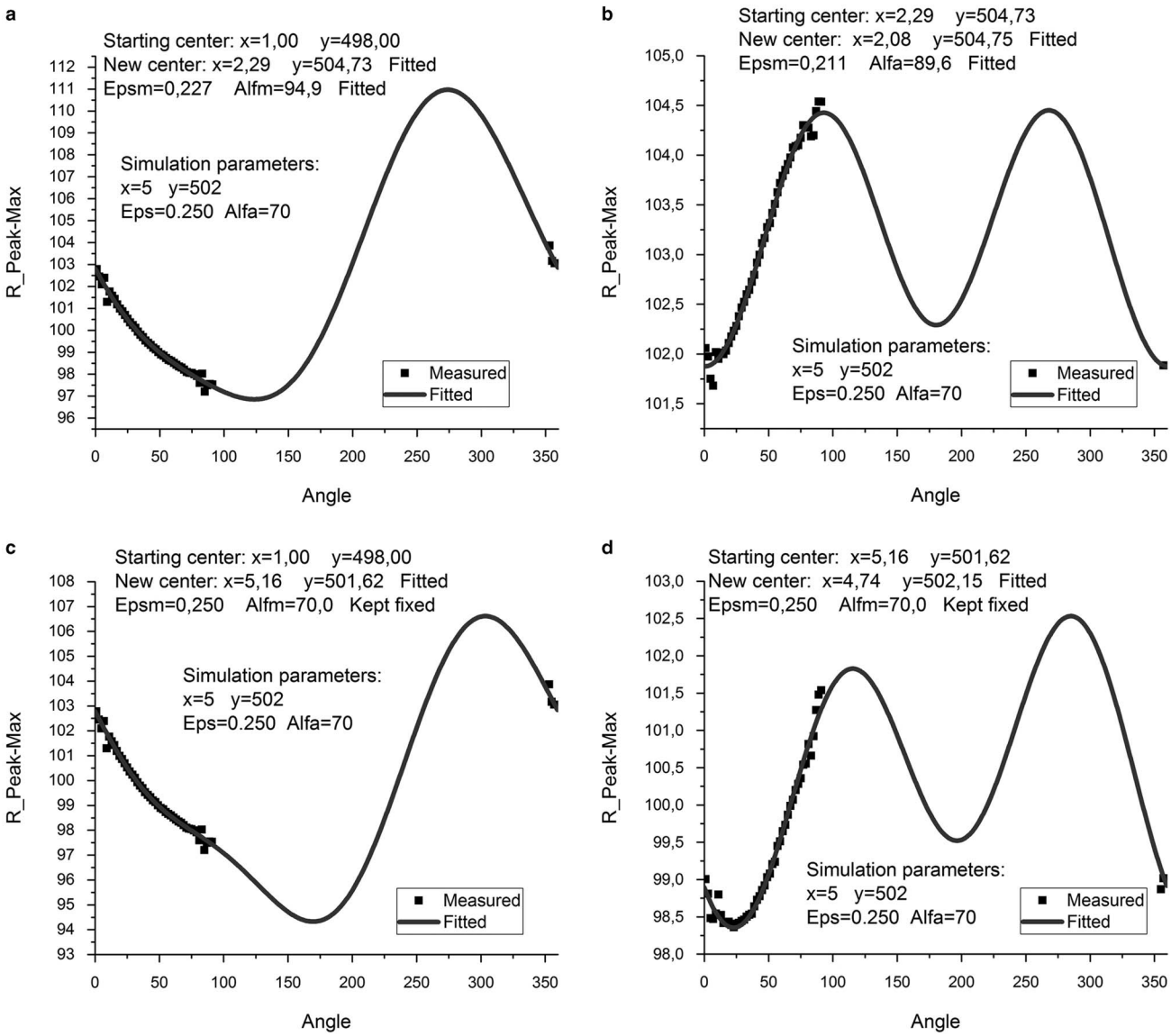

Figure 7. Testing convergence, accuracy, and robustness for a simulated pattern with center at the corner. A two-dimensional pattern, similar to that in Figure 6 was generated with center in the corner of the pattern, so about one-quarter of an ellipse is only present. Both the starting boundary conditions and the results are written on the figures (see text for details). **a,b:** Both the pattern center and the elliptical distortion are determined simultaneously. **c,d:** The known value of the elliptical distortion is kept fixed while the pattern center was fitted. **a,c:** First iteration starting from (the same) slightly incorrectly assumed center. **b:** Second iteration from the result of the first in (**a**). Convergence is proved. **d:** Second iteration from the result of the first in (**c**). Convergence is proved. Sub-pixel precision is achieved in (**a** and **b**). Sub-pixel accuracy and precision are achieved in (**c** and **d**).

Next, the procedure was repeated (started from the same shifted assumed center xc = 1, yc = 498) refining only the center and keeping the known value of the elliptical distortion ($\varepsilon = 0.25$, $\alpha = 70$) fixed during the fit, as shown in Figure 7c. (It corresponds to a situation when the elliptical distortion was calibrated in a full pattern and its value is kept for the partial pattern measured under identical conditions.) It resulted in xc = 5.16 and yc = 501.62, which is again sub-pixel accuracy. When the procedure was re-started from that position it resulted xc = 4.74 and yc = 502.15 as seen in Figure 7d. Both convergence and sub-pixel accuracy are demonstrated with this result.

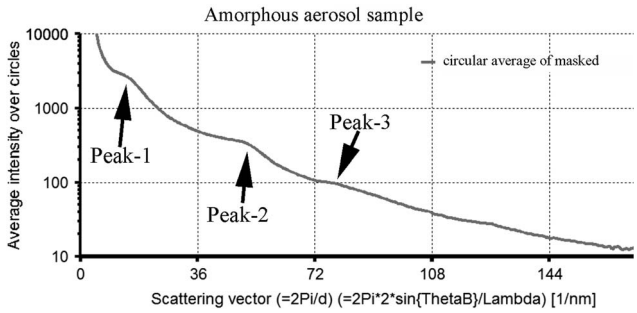

Figure 8. The circularly averaged intensity from Figure 2a over the entire scattering angle range in logarithmic scale. Three diffuse peaks are identified visually.

Test on True Measured Patterns: Robustness and Accuracy

Figure 8 shows the 1D distribution over the entire measured range in logarithmic scale. Three small diffuse peaks are identified visually within this distribution. The second one is selected first to demonstrate the effect of refining the center and distortion simultaneously. During the first test, the center was assumed at $x = 256$, $y = 260$ and both the pattern center and the elliptical distortion were refined. Using an arbitrary manual selection of BKG regions at the two sides of the peak, the refinement gave $dx = 3.2$, $dy = 6.4$, $\varepsilon = 0.250$ and $\alpha = 96°$. After resetting to the same starting conditions, the positions of the BKG points were slightly modified. The refinement resulted in $dx = 3.4$, $dy = 7.6$, $\varepsilon = 0.248$ and $\alpha = 95°$. It shows robustness as far as selection of the BKG points is concerned (within reasonable limits). An example of the starting distributions for a selection of sectors (calculated with the initially assumed center) is shown in Figure 9a, whereas after refinement the

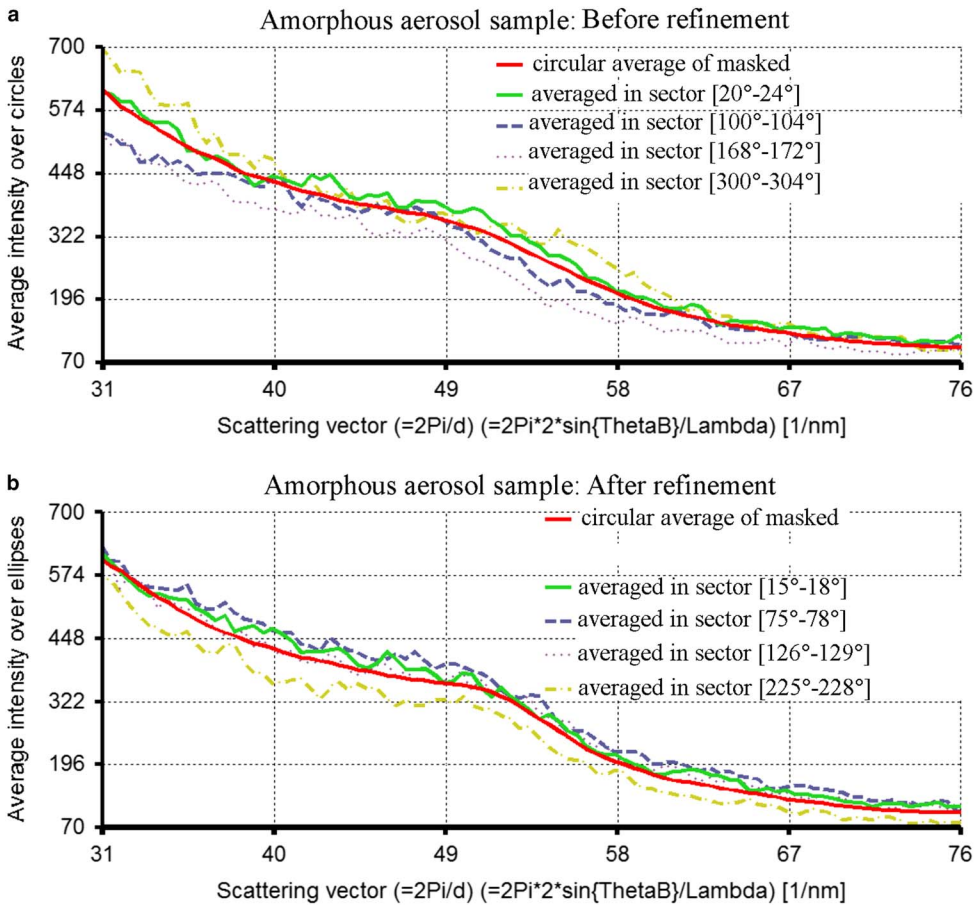

Figure 9. Circularly averaged intensity distribution over the entire circle and for four selected sectors. **a:** Before and (**b**) after the refinement of the center and elliptical distortion. Both scattering of peak positions (among the four sectors shown) and the peak width are reduced due to the refinement.

recalculated distributions for the same sectors are shown in Figure 9b (when the refined center was used for calculating sectors). The quoted values result from a fitting procedure shown in Figure 10a, which demonstrates the measured and fitted angular dependence of the peak positions as a function of the sector's orientation relative to the (right pointing) horizontal line.

In a second test, the refinement was re-started from the newly determined center. Measured and fitted angular dependences are seen in Figure 10b. That refinement resulted $dx = -0.6$, $dy = -0.4$ from the previously refined center together with $\varepsilon = 0.243$ and $\alpha = 95°$. It is seen that the procedure is robust and converges to the same values by sub-pixel accuracy even if it is started from different points of assumed center (starting reasonably close to the true values). The improvement induced by the refinement of the center and of the parameters of the elliptical distortion is proved by the reduced width of the diffuse peak over the BKG. The width of the peak improved to 17 pixels after the refinement (in Fig. 9b) from 21 pixels before the refinement (in Fig. 9a).

Next, a measured pattern with the center at the corner of the CCD was evaluated. Based on the experience with the simulated patterns, the elliptical distortion was separately predetermined for the measurement setup and re-used for a measured diffraction pattern recorded from an amorphous Si_3N_4 thin film with the beam at the corner of the CCD (Fig. 11b). For that purpose, additional full diffraction rings were recorded first from a nc-Ni thin film to precalibrate the elliptical distortion. The measured distances of the selected peak maxima (of the nc-Ni) from the assumed center are shown in Figure 11a together with the fitted curve, which resulted in $\varepsilon = 0.168$ and $\alpha = 42$. These values were kept fixed when the pattern from the amorphous Si_3N_4 sample were processed (Figs. 11c, 11d). In Figure 11c both the effect of the shift in center and of the elliptical distortion are significant and the refinement showed that the center must be shifted by 7 and 4 pixels in the x and y directions from the starting value. To test convergence as a next step, the procedure was re-started from the result of the first refinement and proved to converge to the same center with sub-pixel accuracy. In accordance with that fact, the distribution of distances in Figure 11d is dominated by the elliptical distortion effect alone, but this was kept un-altered from the precalibrated value, resulting in the sub-pixel accuracy.

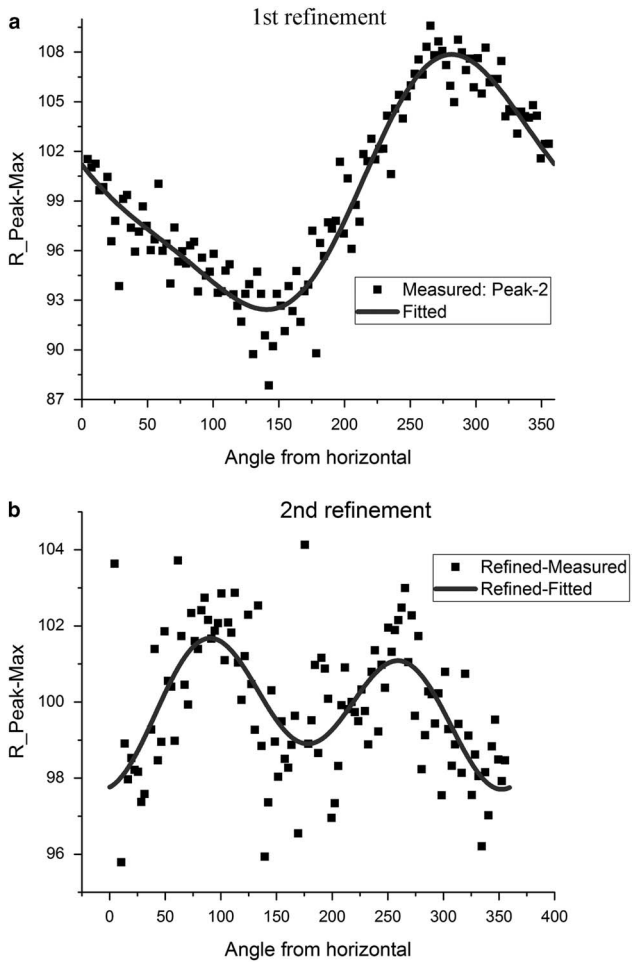

Figure 10. Demonstration of the procedure by fitting to the angular dependence of the peak positions on the direction of the sectors. The distributions from the four sectors in Figure 9 gave 4 points in this figure. The rest is calculated similarly. **a:** First refinement, resulting in $dx = 3.4$, $dy = 7.6$, $\varepsilon = 0.248$, and $\alpha = 95°$. **b:** Second refinement starting from the result of the previous one. The new results are $dx = -0.6$, $dy = -0.4$, $\varepsilon = 0.243$, and $\alpha = 95°$. It shows sub-pixel precision. Convergence is proved.

Limits of the Approaches

Peak-1 and Peak-3 in Figure 8 represent two different limits to the application of the new algorithm. Peak-1 is close to the center. Due to the small size (512 × 512 pixels) of the pattern any one pixel close to the center extends over a "wide-" angular range. For example the circumference of a circle with diameter of 30 pixels is about 90 pixels, resulting in a fact that a single pixel extends in a 4° angular range around the circumference. This is the radius range where the BKG points are selected for Peak-1 at the left side. It is further complicated by the fact that some of those pixels are masked out, so they are missing from the averaging. Consequently, the intensity in the 1D distribution scatters largely from point-to-point for small lengths of the scattering vector. This is illustrated in Figure 12. A few sectors are colored for demonstration in Figure 12a. The 1D distributions calculated by angular averaging within the marked sectors are plotted in Figure 12b. The angular average over the entire circle is smooth, in accordance with our expectations. The mentioned variation of the intensity values prevents us from properly processing Peak-1 sector-by-sector in many sectors. In principle, the angular width of the sector could be increased to alleviate this problem, however, the same act would reduce the number of sectors and consequently the number of points that could be used to fit the angular dependence of the peak position. A compromise must be achieved. A good selection for the sector width seems to be 3–5°, depending on the number of pixels in the pattern and

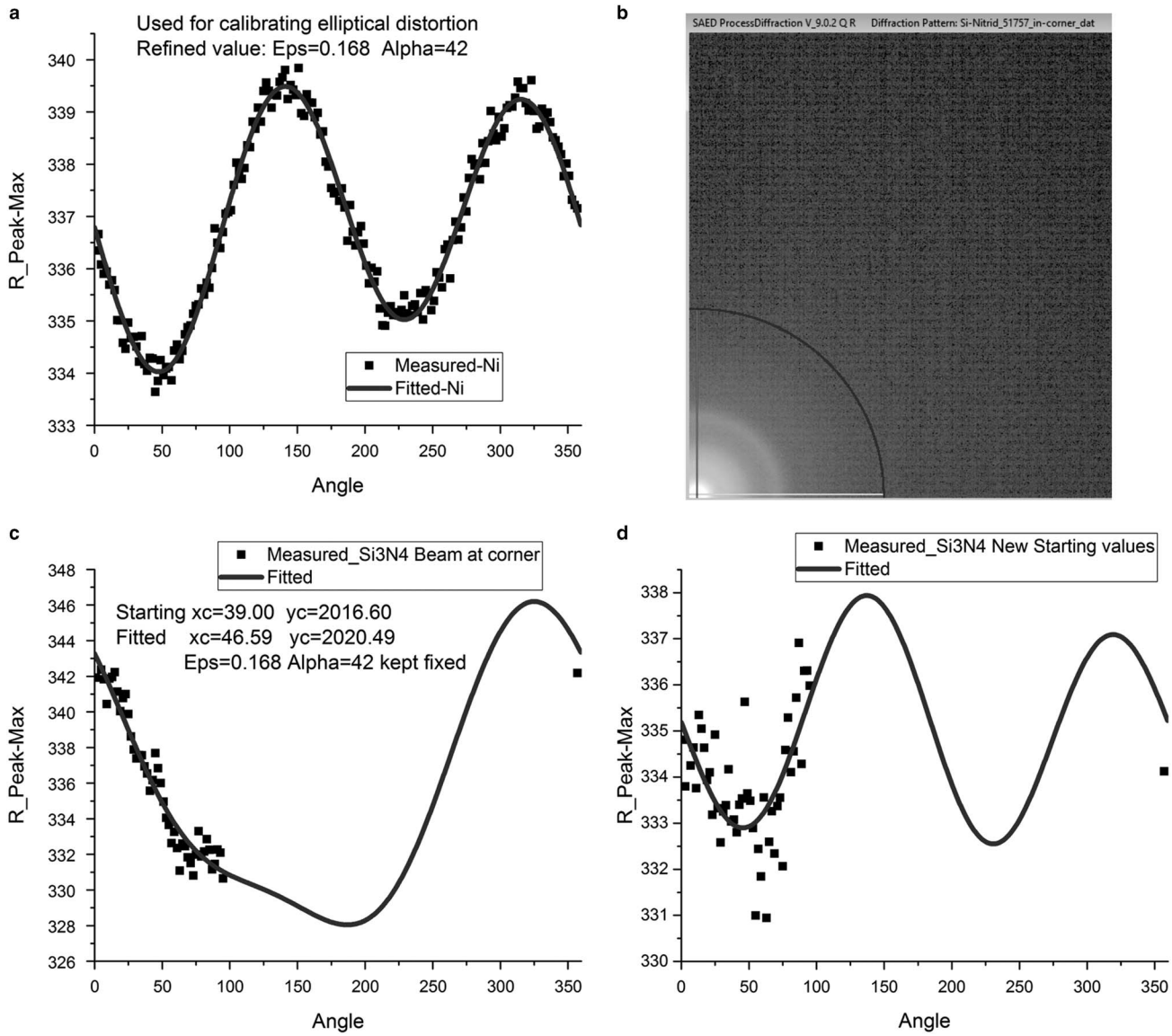

Figure 11. Using precalibrated elliptical distortion in refining the pattern center when the beam is at the corner of the CCD. **a:** A pattern with full rings was recorded from nanocrystalline-Ni thin film to calibrate the elliptical distortion. Angular dependence of peak maxima is shown for the Ni full pattern, which was used to calibrate the actual elliptical distortion of the experimental setup. **b:** Measured pattern from amorphous Si_3N_4 thin film with beam at corner of the CCD under identical experimental conditions as the Ni pattern [used in (**a**)]. Logarithmic intensity scale: rendering is limited to image max = 3,000 counts (to show low intensity parts) while at beam position the measured value is one million counts (resulting from summation of several exposures with different exposure times). **c,d:** Angular dependence of peak maxima from the amorphous Si_3N_4 in (**b**) used to refine the position of the pattern center. The value of elliptical distortion is kept at the value calibrated in (**a**). The procedure is started at two different assumed centers in (**c** and **d**) (see text) and resulted in the same pattern center with sub-pixel precision. The result proves that the procedure is robust for the rough selection of the assumed pattern center.

also on the position of the selected peak (i.e., the radius of the selected circle). The best solution to the problem is to record the pattern with more pixels around the circle of interest (a larger camera with more pixels, less binning or, occasionally, increased camera length).

Peak-3 in Figure 8 poses another problem. The peak is so shallow, even in the circular average over the entire circle, that it is unsurprising that it is lost in the noise when the circular average is calculated over the limited angular range of the sectors only. This means that, although the new algorithm expanded the range of possibilities from well-developed peaks to small diffuse peaks over a steep BKG, which does not show local maxima, it still has its own limits. The small diffuse peak needs to be detectable within the majority of the sectors, too. This limitation can only be overcome by improved statistics.

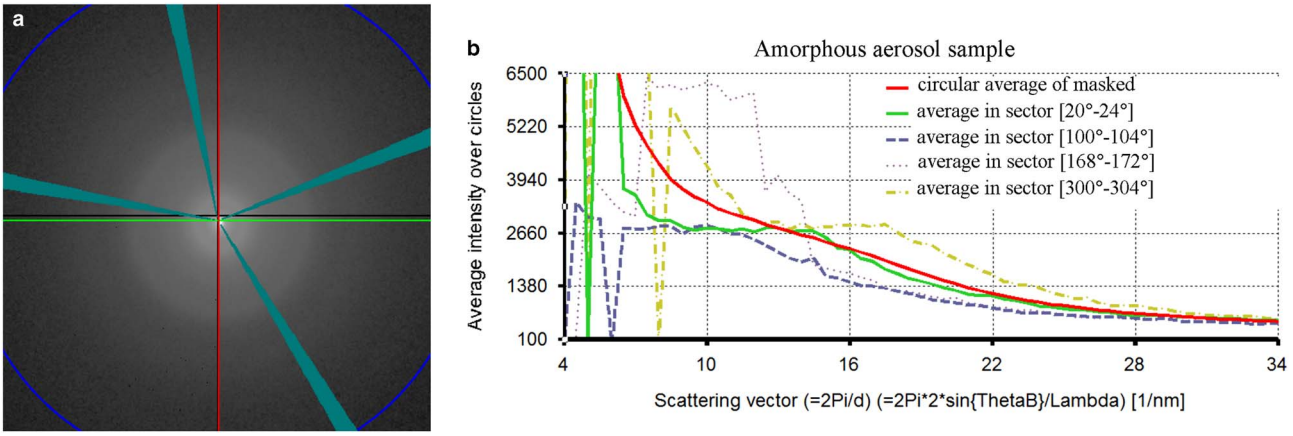

Figure 12. a: Selected sectors are marked in the two-dimensional pattern (512 × 512 pixels). **b:** Circularly averaged distribution form the same sectors that are marked in (**a**) together with the average over the entire circle. The central pixels represent too large angular range. Missing pixels due to mask represent too large angular range of missing data. Consequently, the one-dimensional distributions corresponding to the sectors, start with wildly scattered intensity values hindering smooth processing.

Conclusions

The procedure of refining the assumed pattern center and the parameters of the elliptical distortion is extended to work successfully even on broad diffuse rings on a steeply changing BKG where no local maxima are present at the centers of the rings, which is frequently the case for amorphous materials. These corrections are also important for further processing of such patterns, namely combining the information content of similar patterns, when the low intensity part is lost in the noise, and performing ePDF analysis from the combined pattern. The procedure is based on analytical functions, whose parameters are determined by nonlinear fitting. Even patterns with the beam at the corner of the CCD are successfully processed, provided that the elliptical distortion is precalibrated on full-ring patterns. The procedure starts with manual interaction (rough starting value for the center and selection of two BKG intervals) and lasts about 30 s on a Dell XPS13 Ultrabook (Dell, Round Rock, TX, USA) with Inter Core I5-3337U at 1.8 GHz processor with 8 GB RAM and a 256 GB solid state drive when processing of a 512 × 512 pixel^2 pattern.

Acknowledgments

Useful discussions by Dr. Alejandro Gómez-Pérez are acknowledged. The author is grateful to Péter Barna and Domokos Bíró for providing the TiN–AlN sample. Patterns recorded with the TimePix detector are kindly provided by NanoMEGAS. P.P.D. acknowledges funding support for this research work from European Research Project Eurostars E! 9231.

Financial Support

This research was instigated and financially supported by NanoMEGAS SPRL (Brussels, Belgium) through their ordering TEM diffraction measurements on amorphous materials.

References

Belletti, D., Calestani, G., Gemmi, M. & Migliori, A. (2000). QED V1.1: A software package for quantitative electron diffraction data treatment. *Ultramicroscopy* **81**, 57–65.

Capitani, G.C., Oleynikov, P., Hovmöller, S. & Mellini, M. (2006). A practical method to detect and correct for lens distortion in the TEM S. *Ultramicroscopy* **106**, 66–74.

Carvalho, D. & Morales, F.M. (2012). High-resolution electron diffraction: Accounting for radially and angularly invariant distortions. *Microsc Microanal* **18**, 638–644.

Hou, V.D.-H. (2008). A DigitalMicrograph™ script to characterize elliptical distortion of electron diffraction patterns in TEM. *Microsc Microanal* **14**(Suppl 2), 1124–1125.

Hou, V.D.-H. & Li, D. (2008). A method to correct elliptical distortion of diffraction patterns in TEM. *Microsc Microanal* **14**(Suppl 2), 1126–1127.

Jansen, J. (2006). Structure refinement by taking dynamical diffraction into account. In *Electron Crystallography*, Weirich, Th.E., Lábár, J.L. & Zou, X.D. (Eds.), NATO Science Series II: Mathematics, Physics and Chemistry, vol. 211, pp. 355–372. Dordrecht: Springer.

Klinger, M. & Jager, A. (2015). Crystallographic Tool Box (CrysTBox): Automated tools for transmission electron microscopists and crystallographers. *J Appl Crystallogr* **48**, 2012–2018.

Klinger, M., Nemec, M., Polivka, L., Gartnerova, V. & Jager, A. (2015). Automated CBED processing: Sample thickness estimation based on analysis of zone-axis CBED pattern. *Ultramicroscopy* **150**, 88–95.

Lábár, J.L. (2000). "ProcessDiffraction": A computer program to process electron diffraction patterns from polycrystalline or amorphous samples. In *Proceedings of the 12th European Congress on Electron Microscopy*, Frank, L. & Ciampor, F. (Eds.), pp. I379–I380. Brno: Czechoslovak Society for Electron Microscopy.

Lábár, J.L. (2002). A tool to help phase identification from electron diffraction powder patterns. *Eur Microsc Anal* **75**, 9–11.

Lábár, J.L. (2005). Consistent indexing of a (set of) single crystal SAED pattern(s) with the ProcessDiffraction program. *Ultramicroscopy* **103**, 237–249.

Lábár, J.L. (2008). Electron diffraction based analysis of phase fractions and texture in nanocrystalline thin films, Part I: Principles. *Microsc Microanal* **14**, 287–295.

Lábár, J.L. (2009). Electron diffraction based analysis of phase fractions and texture in nanocrystalline thin films, Part II: Implementation. *Microsc Microanal* **15**, 20–29.

Lábár, J.L. & Adamik, M. (2001). ProcessDiffraction V1.2: New possibilities in manipulating electron diffraction ring patterns. *Microsc Microanal* **7**(Suppl 2), 372–373.

Li, X. (2007). Quantitative analysis of polycrystalline electron diffraction patterns. *Microsc Microanal* **13**(Suppl 2), 966–967.

Mitchell, D.R.G. (2008a). Circular Hough transform diffraction analysis: A software tool for automated measurement of selected area electron diffraction patterns within Digital Micrograph. *Ultramicroscopy* **108**, 367–374.

Mitchell, D.R.G. (2008b). DiffTools: Electron diffraction software tools for DigitalMicrograph™. *Microsc Res Tech* **71**, 588–593.

Mitchell, D.R.G. & Petersen, T.C. (2012). RDFTools: A software tool for quantifying short-range ordering in amorphous materials. *Microsc Res Tech* **75**, 153–163.

Mitchell, D.R.G. & Van den Berg, J.A. (2016). Development of an ellipse fitting method with which to analyse selected area electron diffraction patterns. *Ultramicroscopy* **160**, 140–145.

Press, W.H., Teukolsky, S.A., Vetterling, W.T. & Flannery, B.P. (1996). *Numerical Recipes in FORTRAN 77*. Cambridge: Cambridge University Press.

Székely, L., Sáfrán, G., Kis, V., Horváth, Z.E., Mayrhofer, P.H., Moser, M., Radnóczi, G., Misják, F. & Barna, P.B. (2014). Crossover of texture and morphology in $(Ti_{1-x}Al_x)_{1-y}Y_yN$ alloy films and the pathway of structure evolution. *Surf Coat Technol* **257**, 3–14.

Wu, C.H., Reynolds, W.T., Jr. & Murayama, M. (2012). A software tool for automatic analysis of selected area diffraction patterns within Digital Micrograph™. *Ultramicroscopy* **112**, 10–14.